JOURNAL OF GEOPHYSICAL RESEARCH, VOL. 115, C01003, doi:10.1029/2009JC005337, 2010

Madden-Julian Oscillation and sea level: Local and remote forcing

E. C. J. Oliver[1] and K. R. Thompson[1]

Received 20 February 2009; revised 17 June 2009; accepted 16 September 2009; published 14 January 2010.

[1] The Madden-Julian Oscillation (MJO) is the dominant mode of atmospheric variability in the tropical atmosphere on intraseasonal time scales (i.e., weeks to seasons). This study examines the connection between the MJO and global sea level measured by altimeters over the last 17 years. We first identify regions exhibiting a significant (both statistical and practical) relationship between sea level and the MJO. The first region consists of the equatorial Pacific and western coastal zones of North and South America. Consistent with previous studies, we identify wind-driven equatorially trapped Kelvin waves that propagate eastward along the equatorial Pacific and then transform into coastal trapped waves that propagate poleward along the western coasts of North and South America. The second region includes the shallow waters of the Gulf of Carpentaria (off Australia's north coast) and the adjacent Arafura and Timor seas. Setup by onshore winds is shown to be the dominant physical process. Finally, the northeastern Indian Ocean is shown to be a complex region involving a combination of equatorially trapped Kelvin waves, coastal trapped waves, and westward-propagating Rossby waves exhibiting characteristics of both local and remote forcing. The implications of the results for deep and coastal ocean forecasting are discussed.

Citation: Oliver, E. C. J., and K. R. Thompson (2010), Madden-Julian Oscillation and sea level: Local and remote forcing, *J. Geophys. Res.*, *115*, C01003, doi:10.1029/2009JC005337.

1. Introduction

[2] There is growing interest in extending the range of weather forecasts and ultimately developing a seamless prediction capability that bridges both weather and climate [*Waliser*, 2005]. Understanding variability on intermediate time scales (weeks to months) is critical if this is to be achieved. The Madden-Julian Oscillation (MJO) is the dominant mode of atmospheric variability in the tropics in the intraseasonal band and is arguably the main prospect for predictability on these time scales [*Madden and Julian*, 1972; *Zhang*, 2005]. Most of the energy of the MJO is spread across a range of frequencies with periods between 30 and 90 days and zonal wavenumbers of 1 to 3 [*Wheeler and Kiladis*, 1999]. It is an eastward-propagating phenomenon mainly detectable in outgoing longwave radiation, precipitation and zonal wind in the tropics (especially over the Indian and Western Pacific Oceans). The MJO propagates from its genesis point in the Indian Ocean across the Maritime continent and into the Pacific Ocean after which it weakens but continues to travel eastward before dissipating over the Atlantic Ocean and Africa.

[3] Although the strongest effects of the MJO are experienced in the tropics it does affect atmospheric conditions on a global scale. A general qualitative explanation of how the global atmosphere is affected by the MJO is touched on by *Meehl et al.* [1996] who map distributions of wind anomalies and pressure systems for different phases of the MJO. The MJO has also been linked specifically to rainfall in the Pacific Northwest of the USA [*Bond and Vecchi*, 2003] and to tropical cyclone generation in all three ocean basins [*Hall et al.*, 2001; *Maloney and Hartmann*, 2000a, 2000b]. Furthermore, the MJO has been linked to the extratropics by its connections to high-latitude surface air temperatures [*Vecchi and Bond*, 2004] and, more recently, to the North Atlantic Oscillation [*Cassou*, 2008; *Lin et al.*, 2009].

[4] The Madden-Julian Oscillation is mainly an atmospheric phenomenon but it also has an oceanic expression. Sea surface temperatures have been observed to exhibit characteristics associated with the MJO [e.g., *Woolnough et al.*, 2000; *Shinoda et al.*, 1998]. There have also been observations of large-scale instraseasonal sea level variability in the extratropics (South Atlantic Ocean, South Indian Ocean, and North Pacific Ocean) which were well correlated with wind stress curl [*Fu*, 2003]. This sea level variability was found to be consistent with a basic barotropic vorticity model forced by the global wind field but connections to the MJO were never explored. *Enfield* [1987] used tide gauge data to study intraseasonal oscillations along the Pacific coast of the Americas and *Spillane et al.* [1987] speculated on remote forcing by equatorially trapped waves generated by the MJO. They attributed significant variability to coastally trapped waves that were not obviously forced by local meteorology and were coherent with eastward-propagating

[1]Department of Oceanography, Dalhousie University, Halifax, Nova Scotia, Canada.

0148-0227/10/2009JC005337$09.00

equatorially trapped waves with periods of about 50 days. This area has continued to be an active area of research [e.g., *Clarke and Ahmed*, 1999]. One goal of the present study is to expand on these previous works by including global altimeter observations of sea level. Most studies have focussed on the Pacific Ocean but a few notable works discuss forced intraseasonal variability in the Indian Ocean [e.g., *Moore and McCreary*, 1990; *Han et al.*, 2001; *Sengupta et al.*, 2001; *Iskandar et al.*, 2005]. The relevant aspects of these papers are discussed later.

[5] The theory governing the coastal response to low-frequency equatorially trapped Kelvin waves incident upon an eastern boundary includes subtleties worthy of note. There exists a critical latitude, equatorward of which the incident energy is reflected back into the basin as Rossby waves; poleward of which the incident energy is transmitted poleward as propagating coastal trapped waves [*Grimshaw and Allen*, 1988; *Clarke and Shi*, 1991; *Clarke*, 1992]. For perfectly meridional eastern boundaries, this critical latitude is identical to the turning point associated with Rossby waves in the open ocean [*Cane and Sarachik*, 1981]. Furthermore, using the curved coastline metrics of *Clarke* [1977], it can be shown that for nonmeridional eastern boundaries the critical latitude depends on the orientation of the coastline [e.g., *Clarke and Shi*, 1991]. This dependence is such that the critical latitude is closer to the equator for more inclined coastlines leading to decreased leakage of Rossby waves and increased flux of energy associated with coastal trapped waves.

[6] Our understanding of the dynamics of the MJO comes from observations rather than physical principles or models, both of which perform poorly at consistently explaining and predicting the genesis and evolution of the MJO, its interaction with the extratropical atmosphere and coupling with the ocean. Thus at the present time there remains an important role for empirical studies which use statistical techniques to explore the relationship between the MJO and global distributions of atmospheric and ocean variables.

[7] This paper focuses on the relationship between the MJO and sea level measured on a global grid. Sea level was chosen as the ocean variable of interest for several reasons. First, with the advent of altimeter measurements, it has been continuously mapped on a global scale since 1992 [see *Fu et al.*, 1994; *Cazenave et al.*, 2008]. Second, it is a fundamental variable of interest in its own right and also a variable that can be used to infer, for example, changes in quantities like surface geostrophic flow, heat content and wave propagation. Sea level appears in the momentum equations as a gradient term and is thus a natural integrator of ocean dynamics. Furthermore, it generally has longer coherence scales than other variables such as horizontal currents.

[8] In this study we relate global sea level to the MJO using a scalar metric based on the coherence between the MJO and global sea level averaged across the MJO band. The global perspective allows us to identify regions of the ocean with a particularly strong connection with the MJO. We identify three such regions: the equatorial Pacific and coastal Americas, the Gulf of Carpentaria and the north-eastern Indian Ocean. In a set of regional analyses, we use frequency-dependent statistical techniques to isolate and describe the sea level variability in the MJO band and then attempt to explain the results using simple physical principles and concepts (e.g., wind setup, wave propagation, local and remote forcing).

[9] The paper is structured as follows. The data are presented in section 2 and the statistical methods used to explore connections between sea level and the MJO, and relationships within the sea level data set itself, are described in section 3. In section 4 the global connection between the MJO and sea level variability is described followed by regional analyses in section 5. In section 6 future work is discussed including possible modeling experiments as a means of examining and confirming some of the speculations raised earlier in the paper.

2. Data

2.1. Madden-Julian Oscillation

[10] Daily values of Wheeler and Hendon's bivariate MJO index were obtained from the Government of Australia Bureau of Meteorology (http://www.bom.gov.au/bmrc/clfor/cfstaff/matw/maproom/RMM/index.htm) for the period 1 January 1974 to 31 December 2007. Most of the energy of the MJO has periods between 30 and 90 days, making it a quasi-periodic phenomenon. We will refer to this frequency band as the MJO band. The MJO index is based on the the first two principal components from an empirical orthogonal function analysis of tropical outgoing longwave radiation and zonal winds after removing seasonal and interannual signals [*Wheeler and Hendon*, 2004]. The two indices describe a propagating phenomenon and so they are approximately in quadrature.

2.2. Global Observations of Sea Level

[11] Global fields of satellite-based altimeter measurements of isostatically adjusted sea level anomalies were obtained from Aviso (http://www.aviso.oceanobs.com/en/home/index.html). Weekly data are available on a 1/4° resolution grid which we take over the period from 14 October 1992 to 12 May 2007. For the regional analyses performed in section 5 the data were further processed by spatially averaging to produce a data set with a resolution of 1° (each 4 by 4 block of adjacent points were averaged with equal weights). For both the 1/4° and 1° data sets, time series of anomalies for each spatial grid point were generated by filtering the data using a third-order, high pass Butterworth filter with a cutoff period of 120 days. This generates anomalies that we denote with η_a'. Note that η_a' has had all interannual variability as well as the annual cycle and its first harmonic removed by the filtering.

2.3. Coastal Observations of Sea Level

[12] Measurements of coastal sea level by tide gauges were used to supplement the satellite-based observations. The altimeter does not resolve the coastal sea level well within the Rossby radius of deformation of the coast which decreases from ~150 km in the tropics to ~20 km in the extratropics [*Chelton et al.*, 1998]. Given this limitation, the tide gauge data complements well the observations made by the altimeter. Time series were obtained for thirteen tide gauges along the coast of the Americas (seven south and six north of the equator, for more details see section 5.1) from the University of Hawai'i Sea Level Center (http://uhslc.-

soest.hawaii.edu/). Weekly means were generated from this data set and the resulting time series cover 23 December 1998 to 14 October 2002 (gaps of missing data shorter than 20 days were interpolated). Measurements of sea level pressure, obtained from the NCEP/NCAR Reanalysis (http://www.cdc.noaa.gov/cdc/data.ncep.reanalysis.html) and interpolated to the locations of the tide gauges, were used to remove the inverse barometer effect. The tide gauge data were then high pass filtered as above. The high pass filtered and isostatically adjusted coastal sea level anomalies are denoted by η'_c.

2.4. Global Observations of Surface Wind

[13] Global fields of zonal and meridional surface level winds were obtained from the NCEP/NCAR Reanalysis. Daily fields of global data on a 2.5° grid range from 1949 to 2007 inclusive. In order to facilitate cross-spectral analysis with η'_a the wind data were output as weekly averages and anomalies were generated by high pass filtering as above.

3. Statistical Methods

[14] Two different statistical methods are used to analyze the sea level observations. The first method relates the sea level to the MJO and the second method looks at relationships within the sea level data set. The advantage of the first method is that it uses the MJO index as a surrogate forcing term thus allowing us to explore links between the response (sea level at a specific grid point) and the forcing (MJO). A drawback of using a single index to characterize the MJO is that it has no information on the spatial variability of the MJO. In order to assess the spatial dependence of intraseasonal sea level variability associated with the MJO we supplement the above technique by looking for modes of variability within the sea level data set in the MJO band.

3.1. Relationships Between Sea Level and the MJO

[15] Given a time series of interest, such as η'_a at a particular grid point, how can its relationship with the MJO be quantified? It is possible to explore the relationship between η'_a and the MJO by compositing based on phase and strength of the MJO [e.g., *Hall et al.*, 2001; *Wheeler and Hendon*, 2004; *Vecchi and Bond*, 2004]. One of the strengths of this method is that it allows nonlinear relationships to be resolved. However, compositing of sea level with the MJO index (not shown) has indicated that the assumption of a linear relationship between these variables is reasonable and so traditional time series techniques (e.g., spectral analysis, regression) are used in this study to explore the relationship between sea level and the MJO.

[16] A simple metric was developed to quantify the strength of the relationship between sea level variability and the Madden-Julian Oscillation. It represents the ratio of the variance in η'_a predicted by the MJO (σ_p^2) to the total observed variance in η'_a (σ_o^2)

$$\bar{\kappa}^2 = \frac{\int \kappa^2(\omega) f(\omega) d\omega}{\int f(\omega) d\omega} = \frac{\sigma_p^2}{\sigma_o^2}, \tag{1}$$

where κ^2 is the multiple coherence squared between η'_a and the bivariate MJO index and f is the power spectrum of η'_a. The total observed variance is defined as the integral over f and the predicted variance is the integral over the product of f and κ^2.

[17] The $\bar{\kappa}^2$ statistic reduces the coherency spectra to a scalar value at each spatial point and has the additional useful property that it lies between zero and unity. Similar to coherence, a value of zero implies no relationship (no sea level variance is predicted by the MJO) and a value of unity implies a perfect relationship (all the variance is predicted by the MJO). This metric is more general than a correlation as it allows linear relationships to be found between broad-banded time series even when they are in quadrature (in which case the correlation would be zero). Note that this study generally uses $\bar{\kappa}$ instead of $\bar{\kappa}^2$.

[18] From a practical standpoint a large $\bar{\kappa}$ is not useful unless the predicted response is significant as well. Thus we also use the quantity σ_p, which is the standard deviation of η'_a predicted by the MJO, to assess significance. Regions where both quantities are large implies a significant connection with the MJO. The statistical significance of $\bar{\kappa}$ is assessed using a Monte Carlo method to generate a sample distribution of $\bar{\kappa}$ under the assumption of no relationship with the MJO. Details of the method are given in Appendix A.

3.2. Modes of Sea Level Variability in the MJO Band

[19] Relationships within a spatially distributed data set can be assessed using frequency-dependent empirical orthogonal function (FDEOF) analysis [e.g., *Wallace and Dickinson*, 1972; *Brillinger*, 2001]. This technique allows us to determine the presence of propagating or standing waves within a narrow band of frequencies. This is performed by solving for the eigenmodes of the cross-spectral matrix. This analysis yields a set of complex, frequency-dependent modes which specify the spatial patterns of magnitude and phase relationships within each mode.

4. Global Response of Sea Level to the MJO

[20] The global maps of $\bar{\kappa}$ and σ_p for η'_a are shown in Figure 1. The ocean shows a statistically significant response of sea level to the MJO across the equatorial pacific ($\bar{\kappa} \sim 0.4-0.7$), an intermediate response along coastlines ($\bar{\kappa} \sim 0.3-0.5$) and a weaker but large-scale response in the central North and South Pacific ($\bar{\kappa} < 0.3$). One of the the most notable features is that a much higher fraction of the coastal response is explained by the MJO along the western coastlines than along the eastern coastlines of each landmass (most obvious along the coasts of Sumatra and the Malay Peninsula). This coastal response is strongest along the Maritime Continent ($\bar{\kappa} \sim 0.5$), followed by the Americas ($\bar{\kappa} \sim 0.3-0.5$) and weakest along the coast of west Africa ($\bar{\kappa} < 0.3$). This is consistent with the understanding of the MJO as an eastward-propagating phenomenon which originates, and is strongest, in the vicinity of the Indian Ocean.

[21] The map of σ_p (Figure 1b) is masked according to statistical significance of $\bar{\kappa}$. From this map we can identify several major regions with large $\bar{\kappa}$ and σ_p. First, there is a band along the equatorial Pacific. This region will be treated in detail in an upcoming paper by *Zhang et al.* [2009]. A second region is identified in the northeastern Indian Ocean and includes a complex array of features including coastal

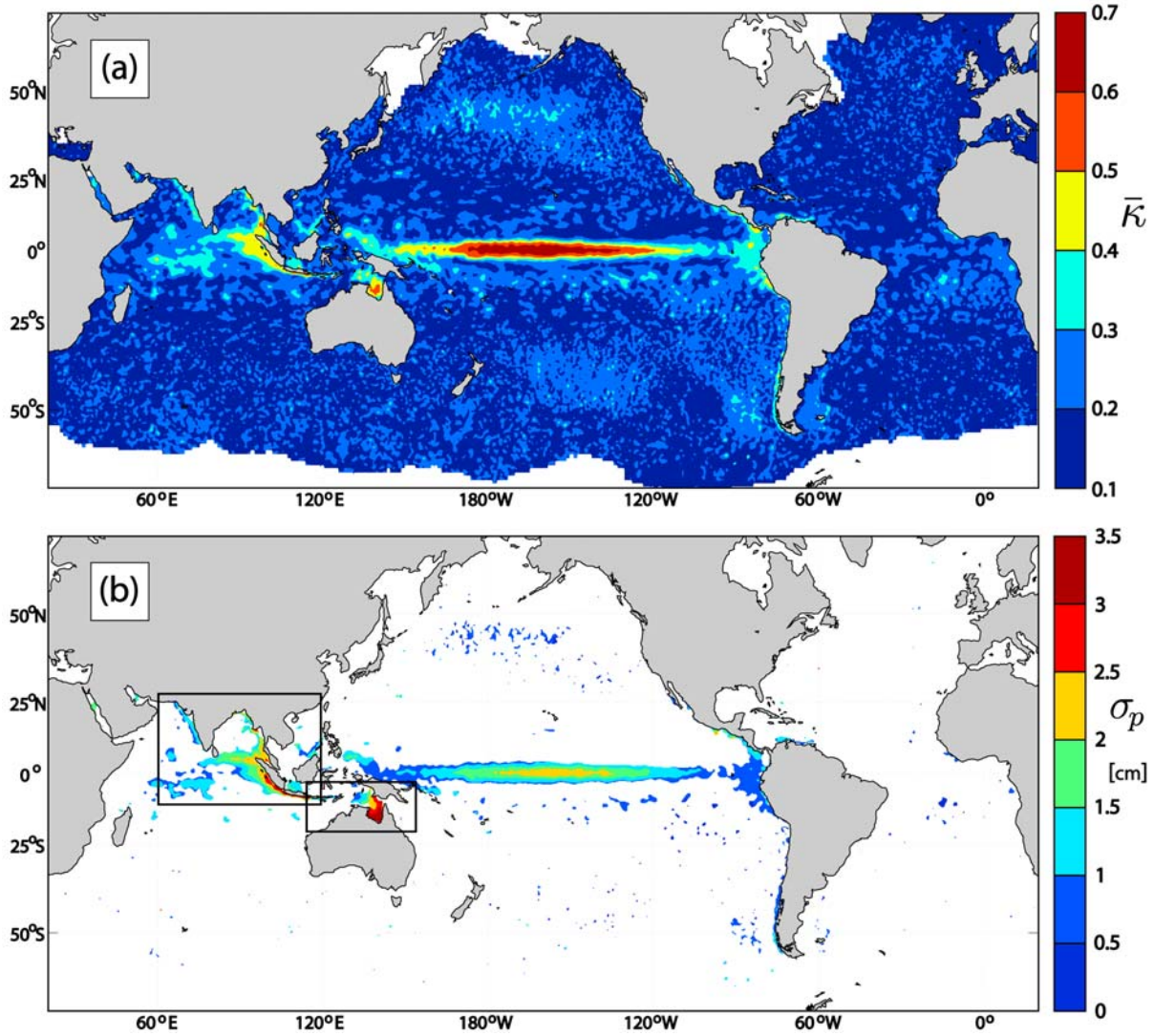

Figure 1. Global maps of the amount of global sea level variability related to the MJO. (a) Here $\bar{\kappa}$, the proportion of the standard deviation of η_a' accounted for by the MJO, is shown. The 5% significance level is $\bar{\kappa}_{5\%} \sim 0.3$. (b) Here σ_p, the magnitude of the standard deviation of η_a' accounted for by the MJO, is shown. The quantity σ_p is only shown for regions where $\bar{\kappa} > \bar{\kappa}_{5\%}$. We can see that the ocean response to the MJO is strongest along the equatorial Pacific but there are also clear responses along the western coasts of the continents and various extratropical regions. The boxes show the study regions examined in sections 5.2 and 5.3.

responses along Sumatra, the Bay of Bengal and the west coast of the Indian subcontinent as well strong signals in the central part of the ocean. A third region covers the Gulf of Carpentaria and the nearby Arafura and Timor Seas, between Australia and New Guinea. Finally, a fourth region is the Pacific coast of the Americas, especially near Central America and tropical South America but also extending to the extratropics along the coast of Chile. As noted above, the altimeter would not resolve the signal near the coast very well in the extratropics. However, we believe the coastal Americas to form a continuous waveguide based on the strong tropical signal, the strong signal near Chile, and the work of previous authors [*Enfield*, 1987; *Spillane et al.*, 1987; *Clarke and Ahmed*, 1999].

[22] Coherence of η_a' and η_c' with the MJO in the identified regions is quantified in Figure 2 (note that the coastal Americas and the equatorial Pacific are combined into one region). The η_c' series were recorded at the coastal tide gauge locations shown in Figure 3 (the exact locations, along with information on time span and completeness, are given in Table 1). (For the equatorial Pacific and coastal Americas analysis, the time series along the coast (both altimeter and tide gauge) constitute 70% of the total variance of the data used in the calculation of coherence withe MJO and so this analysis gives a greater weighting to the coastal signal than to the equatorial signal.) Remarkably, each region shows a peak at a period of about 75 days which suggests that the same large-scale atmospheric forc-

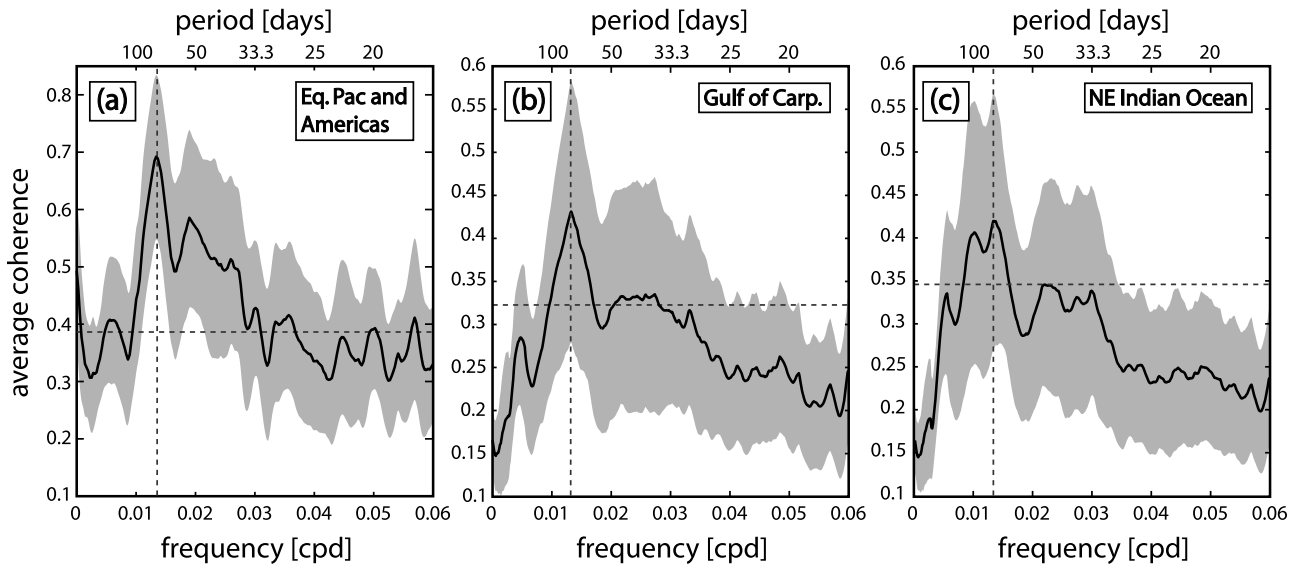

Figure 2. Coherence between the MJO and sea level for three regions. The solid line is the coherence between regional sea level time series and the MJO index averaged over the following regions: (a) the Pacific-Americas waveguide, (b) the Gulf of Carpentaria, and (c) northeastern Indian Ocean (the latter two regions are defined by the boxes in Figure 1b). For each region there is clear maximum at about a period of 75 days (shown by a vertical dashed line) which is used as the frequency for the subsequent FDEOF analysis. The grey band indicates the standard deviation of coherence values within a region. The dashed line shows the 5% significance level based on the degrees of freedom of the individual cross-spectral estimators.

ing may be responsible for driving the variability observed in each region.

5. Regional Responses of Sea Level to the MJO

[23] Sections 5.1–5.3 describe the sea level variability in the three regions mentioned in section 4 and explain it in terms of simple physical processes.

5.1. Equatorial Pacific and Coastal American Waveguides

[24] Figure 3 shows a map of $\bar{\kappa}$ focusing on the eastern equatorial Pacific and the coastal Americas between 50°N and 50°S. There are indications that the sea level response reaches into the extratropics (with decaying magnitude and zonal extent in the poleward direction). A possible physical explanation is that the atmospheric component of the MJO generates equatorially trapped waves in the western Pacific which propagate eastward along the equator before reaching the coastal boundary at which point the energy is reflected as Rossby waves at low latitudes and transferred to poleward-propagating coastally trapped waves at higher latitudes [*Spillane et al.*, 1987; *Clarke and Ahmed*, 1999]. For the Americas on instraseasonal time scales, this critical latitude occurs between 8.5° and 11° from the equator (calculated following *Clarke and Shi* [1991]). These latitudes are consistent with the region of significant seaward extend of $\bar{\kappa}$ in the tropics off the coast of the Americas. Also, the poleward reduction in seaward extent is consistent with Rossby radius of deformation which decreases poleward and defines the length scale for coastal trapping.

[25] A FDEOF analysis was performed on η_a' and η_c' to test the theory that the coastal response is related to waves traveling along the equator and coastlines. The η_a' series were recorded at 25 equally spaced points along the equator from 155°E to 85°W, and 44 near coastal points along the coast of the Americas from 45°S to 44°N (equally spaced in latitude). Note that the tide gauge data were made into weekly averages and that the range η_a' was shortened to match that of η_c' (23 December 1998 to 14 October 2002). Also, the time series were scaled such that the total variance of the equatorial set is equal to the total variance of the coastal set. This ensures that the both the equatorial signal and the coastal signal are weighted equally in the statistical analysis.

[26] The proportion of spectral density accounted for by the first twenty FDEOF modes is shown in Figure 4. This analysis was performed at a frequency corresponding to a period of about 75 days which is the location of the peak in coherence between sea level and the MJO (Figure 2a). The first mode accounts for approximately two-thirds of the total spectral density (defined as the trace of the cross spectral matrix) and the higher-order modes add less than 10% each.

[27] Figure 5 shows the first mode from the FDEOF analysis. Figure 5 (top) shows the magnitude of this mode and Figure 5 (bottom) shows the time delay of the mode (which was derived from the phase of the mode) as functions of "distance" along the waveguides. Distance was calculated along two branches: both run along the equator but split into north and south paths at the coastal boundary. This calculation is made under the assumption that some energy will travel north and some will travel south once the equatorially trapped energy reaches the coastal boundary thus splitting the energy along two paths. The time delay was calculated from the phase of the

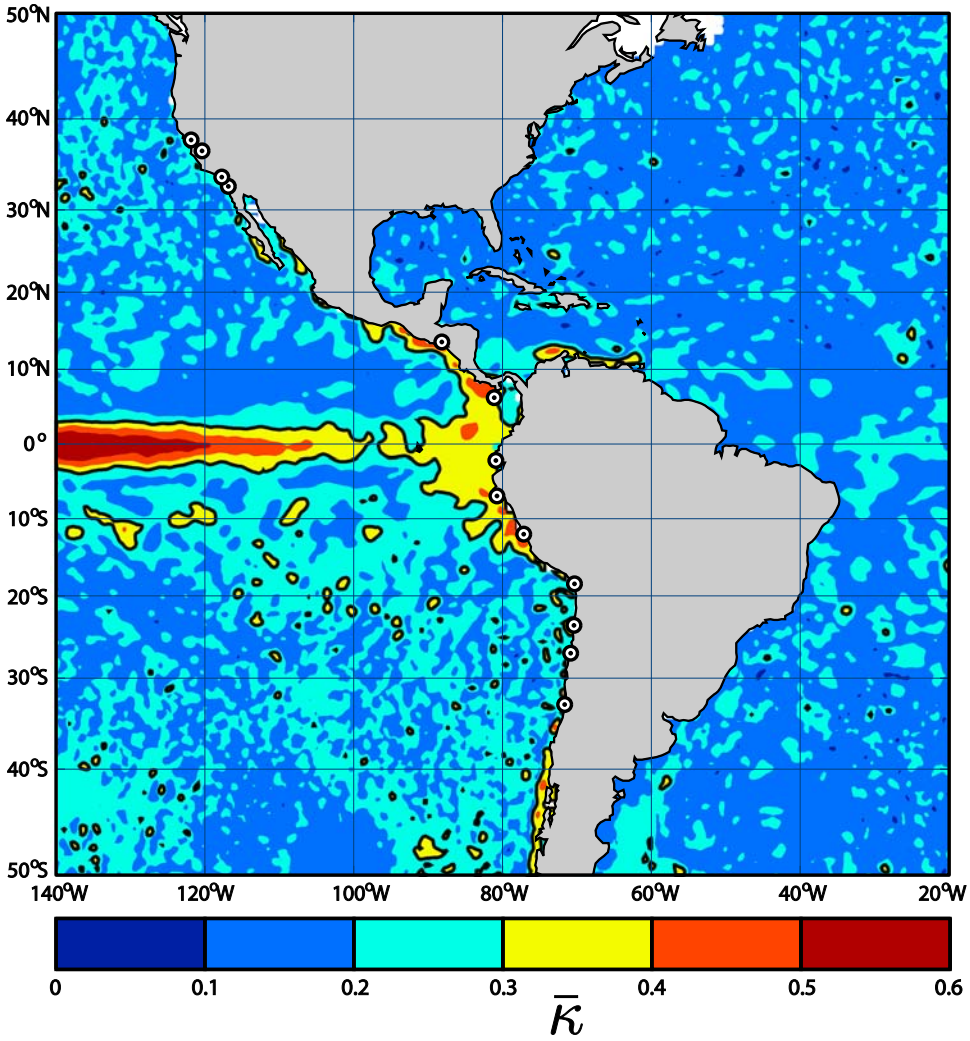

Figure 3. Proportion of sea level variability accounted for by the MJO near the Americas (a regional blowup of Figure 1a). Here $\bar{\kappa}$ represents the fraction of standard deviation of η_a' predicted by the MJO. The 5% significance level (see Appendix A) is $\bar{\kappa}_{5\%} \sim 0.3$ and is denoted by the black contour. The dots show the locations of the coastal tide gauges providing records of η_c' (see Table 1 for detail on each tide gauge).

eigenvector and the time scale of 75 days (the most westerly station is assumed to be $t = 0$).

[28] The time delays shown in Figure 5 are consistent with a response propagating eastward across the equator which excites coastally trapped waves that move poleward along the coast of the Americas. From the linear regression of phase lag on distance we estimate the equatorial wave to have a speed of 2.6 ± 0.1 ms^{-1} which is consistent with the first baroclinic mode of equatorially trapped oceanic Kelvin waves [*Gill*, 1982; *Hendon et al.*, 1998; *Zhang et al.*, 2009]. The coastal waves have speeds of 5.6 ± 2.6 ms^{-1} (Northern Hemisphere) and 3.3 ± 0.6 ms^{-1} (Southern Hemisphere). Error bounds were determined from the distribution of linear fit parameters based on 10,000 fits using bootstrap resampling. The speeds found here are similar to those found by *Brink* [1982] who developed a semitheoretical model for free, coastally trapped long waves (with periods from a few days up to 20 days). Also, our measure of wave speed along the coast of South America is consistent with the speed obtained from the model developed by *Clarke and Ahmed* [1999]. The amplitude increases slightly with distance eastward along the equator. According to theory, the sea level amplitude of the coastal trapped wave should increase as $\sqrt{|f|}$ due to flux conservation [*Clarke*, 1992];

Table 1. Details on the Tide Gauge Records[a]

Name	Latitude	Longitude	Percent Complete
San Francisco	37°48′N	122°28′W	100
Monterey	36°36′N	121°53′W	99.3
Los Angeles	33°43′N	118°16′W	100
San Diego	32°42′N	117°10′W	99.8
Acajutla	13°35′N	89°50′W	99.2
Armuelles	6°16′N	82°52′W	99.9
La Libertad	2°12′S	80°55′W	99.4
Lobos	5°56′S	80°43′W	99.6
Callau	12°3′S	77°9′W	99.7
Arica	18°28′S	70°20′W	99.9
Antofagasta	23°39′S	70°24′W	94.6
Caldera	27°4′S	70°50′W	99.5
Valparaiso	33°2′S	71°38′W	98.4

[a]The completeness percentage is over the common period from 23 December 1998 to 14 October 2002.

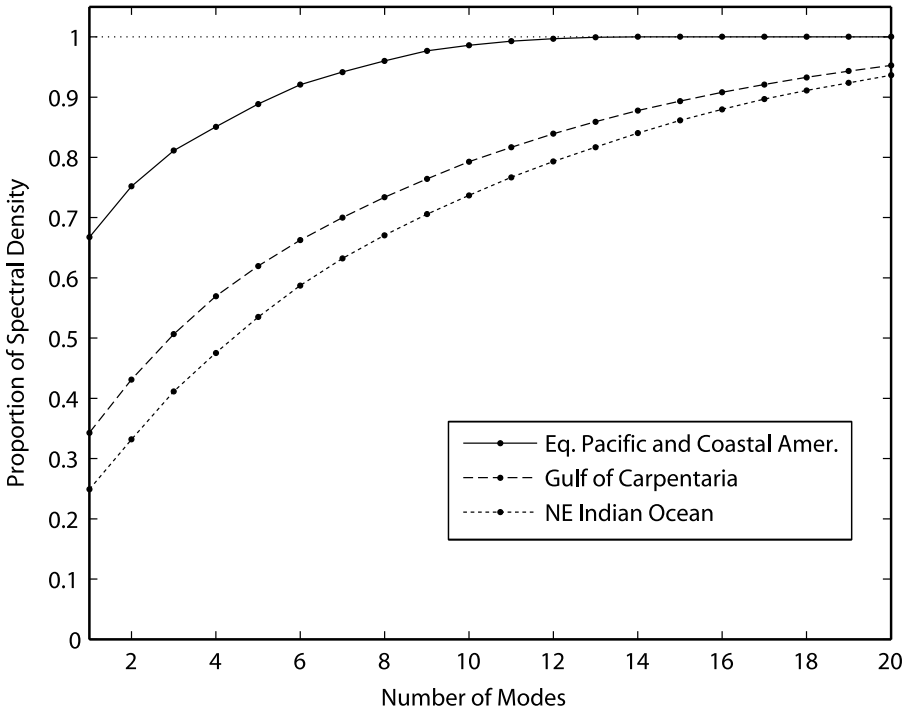

Figure 4. Total spectral density accounted for as a function of the number of modes included. The vertical axis is fraction of the spectral density at a 75 day period accounted for by the FDEOF modes and the horizontal axis represents the number of modes included. In each case the first mode dominates the results although its relative strength compared to higher-order modes is much stronger in the Pacific-Americas region. The maximum number of modes, for which the proportion of spectral density reaches unity, is equal to the number of time series used in the FDEOF analysis: 82 for the equatorial Pacific and coastal Americas, 555 for the Gulf of Carpentaria, and 1814 for the northeastern Indian ocean.

substantially less so if the effects of topography and friction are included [*Clarke and Ahmed*, 1999]. However, along the coastal boundaries the amplitude has too much scatter to make a definitive conclusion as to the trend. As discussed previously, outside the tropics the sea level signals within a Rossby radius from the coast are not well resolved by the altimeter measurements. This may explain the large amount of scatter in the middle- and high-latitude altimeter points in the delay of the mode (Figure 5). It may be possible to obtain a more accurate measure of wave speed by omitting the altimeter data at higher latitudes but the small number of points would make the sample size too small to give much confidence in the results.

[29] Similar intraseasonal poleward traveling coastally trapped waves along the coast of the Americas were studied by *Spillane et al.* [1987]. They examined relationships between time series of sea level height from coastal tide gauges. *Spillane et al.* [1987] found a coherent wave with a period between 47 and 58 days traveling poleward from the equator to 55°N and 15°S. Over the range 10°N to 40°N the wave has a nearly constant speed of $\sim$1.7 ms^{-1} which is slower that our estimate (although the wave has a different time scale). A followup study examined possible forcing reaching the coastal Americas by way of the equatorial Pacific ocean [*Enfield*, 1987] and found that there is a coherent wave that travels along the equatorial Pacific and the coast of the Americas. They concluded that the forcing occurred remotely in the western Pacific. Our analysis expands on the work of *Enfield* [1987] and *Spillane et al.* [1987] by including satellite-based measurements of sea level in addition to tide gauges and by making a statistical connection with the MJO which we treat as a surrogate for forcing.

5.2. Gulf of Carpentaria

[30] In order to explain the high values of $\bar{\kappa}$ in the Gulf of Carpentaria, the FDEOF technique is applied to sea level data within a region surrounding northern Australia (see box in Figure 1b). The frequency at which the FDEOF analysis is carried out corresponds to a period of 75 days (see Figure 2b).

[31] The first mode accounts for 34% of the total spectral density (see Figure 4). Maps showing the cyclic evolution of the first mode are given in Figure 6. This mode primarily describes a standing wave of sea level in the relatively shallow Gulf of Carpentaria and the nearby Arafura and Timor Seas to the west (see Figure 6). Weaker progressive waves are also evident in the deeper water off the northwestern and northeastern Australian coasts.

[32] The standing wave may be due to the effect of wind setup over the shallow waters noted above. To explore this possibility we will first examine the sea level variability at the head of the Gulf of Carpentaria. Sea level at the head of the Gulf (the southeastern end), η_H, is taken as the average of the five points whose locations are depicted in Figure 6. A plot of this time series over a selected time period is shown in Figure 7. Figure 7a shows η_H and we see variations on the order of 60 cm including a strong seasonal cycle. Figure 7b shows the same data after removing the

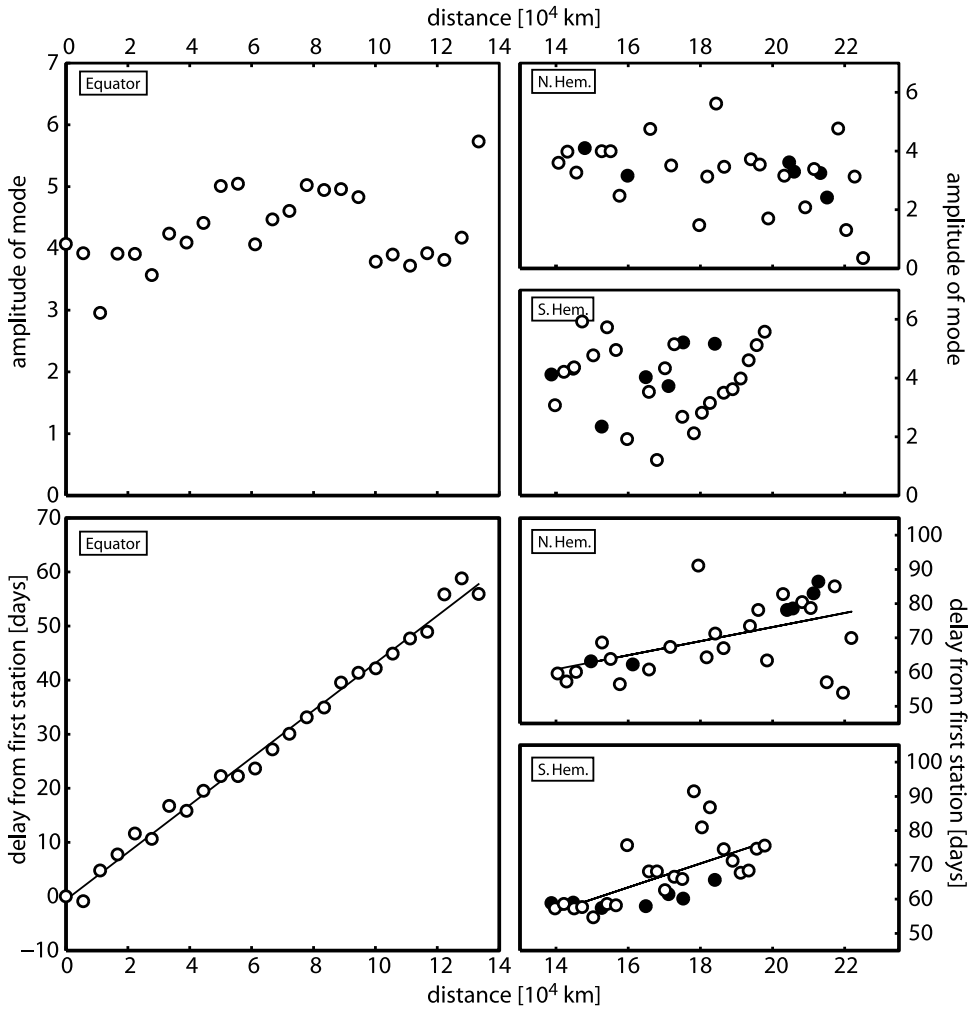

Figure 5. The first mode of the FDEOF analysis for the Pacific-Americas waveguide, explaining 67% of the variance, at a period of 75 days ((top) magnitude of response and (bottom) time delay from first station). Open circles represent satellite data and solid circles represent tide gauge data. The equator, Northern Hemisphere coast, and Southern Hemisphere coast are split for visual clarity. The lines in Figure 5 (bottom) represent linear regressions with slopes representing wave speeds of 2.6 ± 0.1 ms^{-1} (equator), 5.6 ± 2.6 ms^{-1} (Northern Hemisphere), and 3.3 ± 0.6 ms^{-1} (Southern Hemisphere).

seasonal cycle (annual and semiannual cycles were removed by harmonic regression). Much of this variability is concentrated in the MJO band which is emphasized in the 30–90 day band-passed series shown in Figure 7c.

[33] The prediction of the sea level anomaly at the head of the Gulf of Carpentaria due to wind setup, $\hat{\eta}_H$, was calculated as follows. Assuming constant density and depth, and steady state, the linearized momentum equations representing the ocean response to wind forcing leads to a balance of surface wind stress, τ, and the pressure gradient along the gulf (which we took to be northwest-southeast, based on the shape of the standing mode in Figure 6 and the local shape of the coastline). We chose the head of the gulf to be in the southeast corner (see Figure 6) and defined the length to be L = 1000 km. We acknowledge that this value is somewhat subjective and open to uncertainty. The averaging period for the sea level is one week and this is much longer than the time estimated to reach a steady state (~1 day). It follows that setup theory can be applied independently at each point in time to predict the sea level response to wind stress. Assuming the sea level change at the "mouth" is zero, this leads to the following expression for the sea surface height at the head

$$\hat{\eta}_H = \frac{L\tau}{\rho g h}, \tag{2}$$

where g is gravitational acceleration (9.8 ms^{-3}), ρ is the density of seawater (taken to be 1024 kg/m^3) and h is the water depth (36 m, based on ETOPO2 bathymetry data obtained from http://www.gfdl.noaa.gov/products/vis/data/datasets/etopo2_topography.html). The along gulf wind component, w, was calculated from the average of all northwesterly winds in the box shown in Figure 6. The wind stress was calculated using $\tau = \rho_a c_d(a) a w$, where ρ_a is the density of air (taken to be 1.2 kg/m^3), $c_d(a)$ is the wind-dependent air-sea drag coefficient and a is a modification of the wind speed to account for the contribution to the stress from variability lost by taking a weekly average of the daily

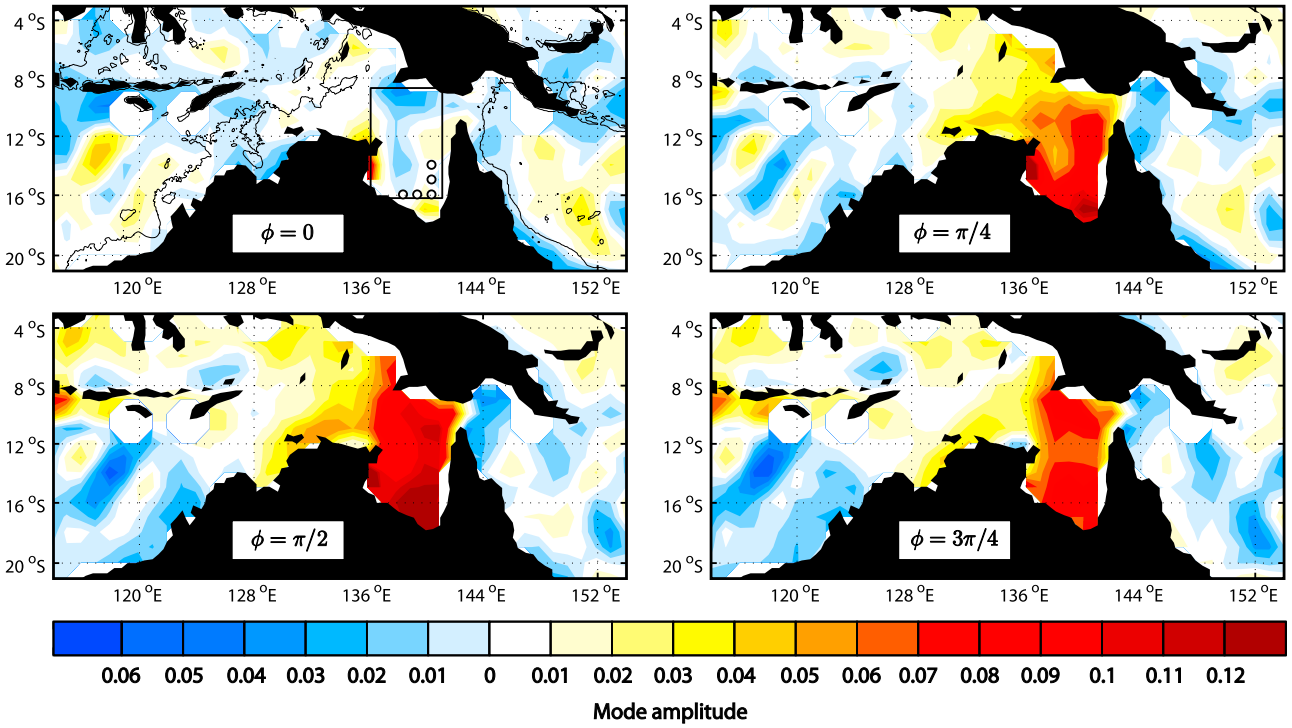

Figure 6. Maps of the first FDEOF mode (34% of the variance) in the Gulf of Carpentaria region for one half of its cycle (in $\pi/4$ radian steps). The complete cycle can be constructed by repeating these snapshots with positive and negative values switched. The mode is dominated by a standing wave in the Gulf of Carpentaria as well as smaller amplitude traveling waves to the east and west of Australia. Note that given the period of the mode is 75 days, the above sequence has a time range of 32.5 days. In order to show the shallow waters of the Gulf of Carpentaria and the Arafura and Timor seas a thin black line representing the 100 m bathymetric contour is shown. The box shows the region for the wind field (8.75°S–16.25°S and 136.25°E–141.5°E) and the circles show the locations of sea level time series used in the setup analysis ([16°S, 138.5°E], [16°S, 139.5°E], [16°S, 140.5°E], [15°S, 140.5°E], and [14°S, 140.5°E]).

winds (see *Thompson et al.* [1983] for details on the calculation of a).

[34] The predicted sea level setup, $\hat{\eta}_H$, is plotted in Figure 7a along with the aforementioned time series of η_H. Figures 7b and 7c show the observed sea level and setup after removing the seasonal cycle (as above) and applying a 30–90 day bandpass filter, respectively. It is clear that the wind setup explains most of the seasonal cycle as well as several large events in the original data; it is particularly powerful at predicting the band-passed sea level variability. Quantitatively, the zero lag cross correlation between the band-passed sea level and setup is 0.70. However, the model overestimates the sea level significantly (the minimum RMS difference between η_H and $\hat{\eta}_H$ is found for $0.57\hat{\eta}_H$). At a period of 75 days the coherence between the band-passed η_H and $\hat{\eta}_H$ (effectively the wind stress) is 0.79 (between 0.5 and 0.8 across the entire MJO band with a 5% significance level of 0.28). Sea level setup therefore explains a large portion of sea level variability at the head of the gulf and is especially relevant on MJO time scales.

[35] Note the multiple coherence between the northwesterly wind stress and the MJO index is 0.68 at a period of 75 days (between 0.4 and 0.7 across the entire MJO band with a 5% statistical significance level of 0.25). From this result we conclude that the intraseasonal sea level variability in the Gulf of Carpentaria region is mainly due to the MJO through its influence on local sea level setup.

5.3. Northeastern Indian Ocean

[36] We applied the FDEOF technique to a region in the northeastern Indian Ocean bounded by the box shown in Figure 1b. As above, the 1° resolution η'_a data was used and the frequency, corresponding to a period of 75 days, was chosen based on the peak in average coherence between sea level and the MJO for this region (see Figure 2c). The first mode accounts for 25% of the total spectral density at 75 days (see Figure 4) and its time variation is visualized in Figure 8.

[37] Our interpretation of this mode is that it represents a mixed set of dynamics. It is clear from Figure 8 that there there are relatively fast waves traveling eastward along the equator which strike the western coast of Sumatra. This energy is then reflected back into the basin at low latitudes as Rossby waves or carried poleward at higher latitudes by coastal trapped waves moving south along the coasts of Sumatra and Java and north around the Bay of Bengal. This phenomenon is similar to that observed in the Pacific Ocean (see section 5.1) and and consistent with observations of coastally trapped waves in the Southern Hemisphere along the coasts of Sumatra and Java [*Clarke and Liu*, 1993;

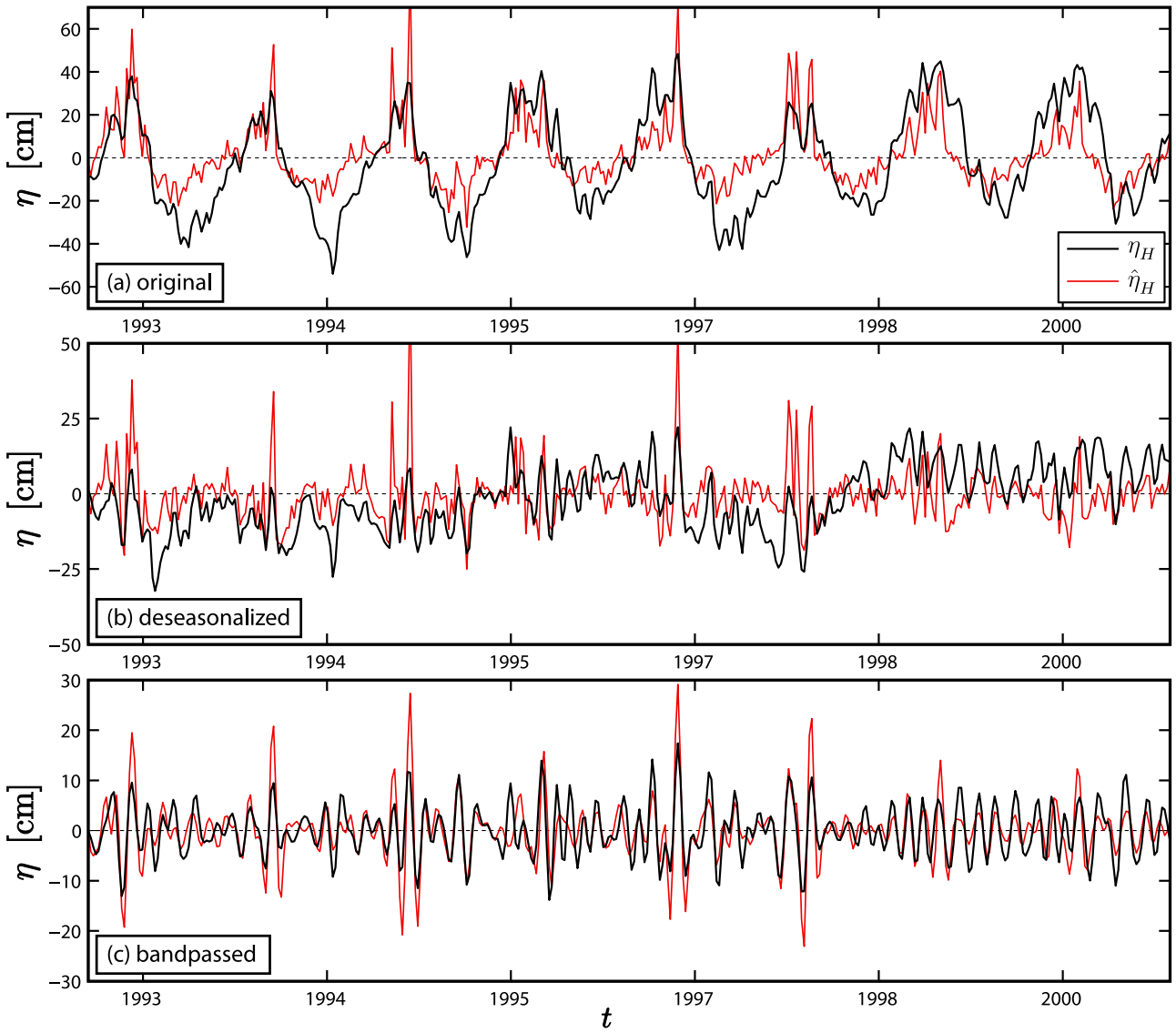

Figure 7. Sea level and local wind setup in the Gulf of Carpentaria. The sea level anomaly at the head of the Gulf of Carpentaria ($\eta_H(t)$) and the wind setup ($\hat{\eta}_H(t)$) are both shown over a selected time period. (a) The sea level at the head and the setup calculated using the original wind stress. (b) The deseasonalized $\eta_H(t)$ and $\hat{\eta}_H(t)$ and (c) the band-passed (30–90 days) $\eta_H(t)$ and $\hat{\eta}_H(t)$. There is good agreement particularly in the timing and sign of the predicted setup response.

Iskandar et al., 2005]. We observe that the Rossby waves are most prominent in the Northern Hemisphere, forming near the tip of Sumatra and propagating along 5.5°N. For a coastline angle of 45° (approximately the coastline angle of Sumatra) and a period of 75 days, the critical latitude is ~9°N which is poleward of the northern tip of Sumatra. Therefore, these Rossby waves are permissible and are consistent with observations by *Chelton et al.* [2003] though it is not clear why they are not observed further north or further south of 5.5°N. In order to illustrate this we have generated a modified Hovmüller diagram (see Figure 8) of η'_a showing the continuous propagation of signals and westward reflection in the tropical Indian Ocean. The horizontal axis of the Hovmüller diagram represents the path of a wave in three sections: (1) eastward along the equator from 50°E (near Africa) to 99°E (Sumatra), (2) northwestward along the coast of Sumatra from the equator to 5°N, and (3) westward along 5.5°N from 94°E to 70°E (this path is shown in Figure 8).

[38] Part of the Hovmüller diagram for a subset of the full time period is shown in Figure 9. This diagram shows that there is continuity between the eastward-propagating signals along the equator and those which propagate westward along 5.5°N. The eastward-propagating component in the

Figure 8. Maps of the first FDEOF mode (25% of the variance) in the northeastern Indian Ocean region for one full cycle (in $\pi/4$ radian steps). The mode shows an equatorially trapped wave striking the western coast of Sumatra and exciting westward-propagating waves around 5.5°N and 5.5°S. There are also indications of coastal trapped waves in the Bay of Bengal. A full cycle is completed in 75 days.

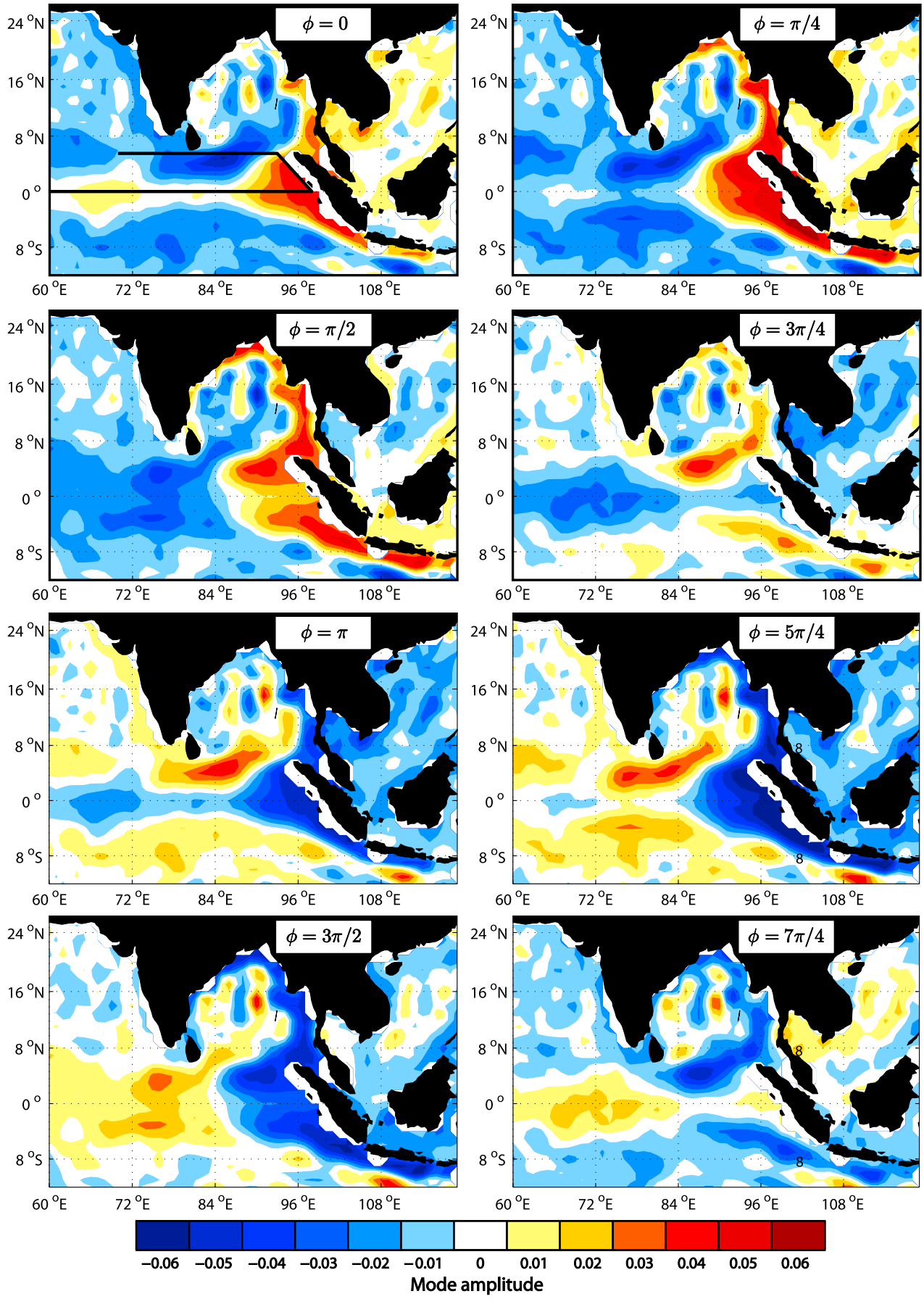
$\phi = 0$
$\phi = \pi/4$
$\phi = \pi/2$
$\phi = 3\pi/4$
$\phi = \pi$
$\phi = 5\pi/4$
$\phi = 3\pi/2$
$\phi = 7\pi/4$
24 °N
16 °N
8 °N
0 °
8 °S
60 °E
72 °E
84 °E
96 °E
108 °E
−0.06 −0.05 −0.04 −0.03 −0.02 −0.01 0 0.01 0.02 0.03 0.04 0.05 0.06
Mode amplitude

Figure 8

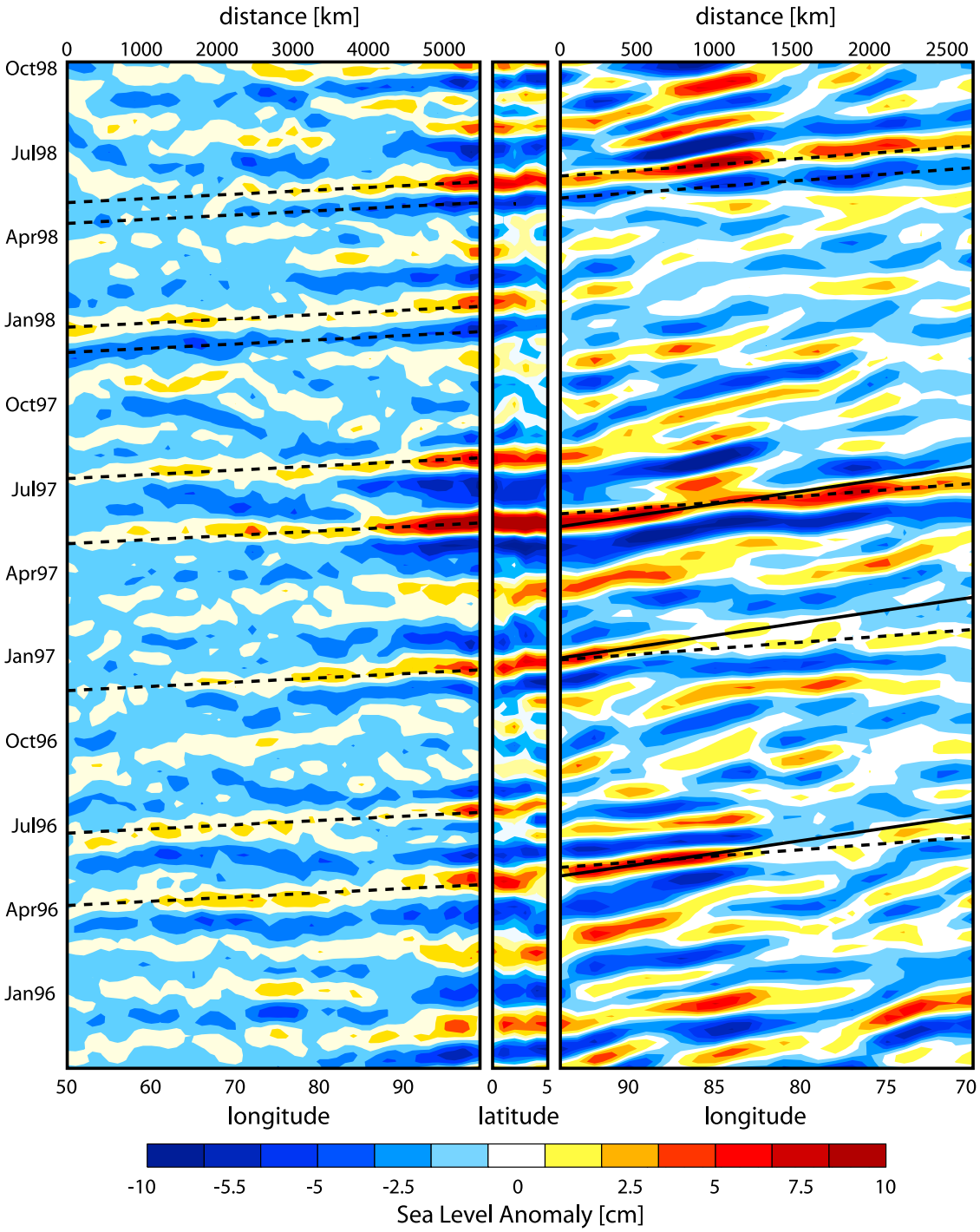

Figure 9. Modified Hovmüller diagram for η_a' for the period from October 1995 to October 1998. The longitude axis is split into the following three regions: (1) eastward along the equator, (2) northwestward along the coast of Sumatra, and (3) westward along 5.5°N. The propagation of signals along the equator and reflection from the eastern boundary is evident. The lines represent wave speeds of 2.8 ms^{-1} in the first section representing the first mode baroclinic Kelvin wave and 0.933 ms^{-1} and 0.467 ms^{-1} in the third section (solid and dashed lines, respectively) representing the first two Rossby wave modes.

first portion of the diagram is consistent with a first mode baroclinic Kelvin wave. In order to illustrate this, a line corresponding to a wave speed of 2.8 ms^{-1} (speed of the first baroclinic mode for equatorial oceanic Kelvin waves in this region [*Chelton et al.*, 1998]) is shown. As noted above, the westward-propagating component appears to be the result of Rossby waves forming off the coast of Sumatra and traveling along 5.5°N. We have added lines to Figure 9 demonstrating the predicted paths of the first two baroclinic Rossby wave modes (speeds of 0.93 m/s and 0.47 m/s, respectively). Our observations are consistent with *Chelton et al.* [2003] who discuss an observed maximum in the

westward-propagating Rossby wave signal near 5.5°N and phase speeds between 0.5 ms^{-1} and 1 ms^{-1}. *Chelton et al.* [2003] also state that theoretically these waves should be associated with identical waves traveling westward along 5.5°S but also note that observations usually identify the waves in the Southern Hemisphere (if they are identified at all) as having much smaller amplitude. The results given by *Chelton et al.* [2003] are consistent with our observations in which we see a slight indication of these waves developing in the Southern Hemisphere but they do not propagate far into the ocean interior. A possible explanation is as follows. The more meridional a coastline, the more poleward is the critical latitude which delineates the change between reflected Rossby waves and coastally trapped waves. The tropical eastern boundary of the Indian Ocean is more meridional in the Northern Hemisphere (Sumatra and Myanmar) than in the Southern Hemisphere (Sumatra and Java) and so the critical latitude will be more poleward in the north than in the south. This will result in more energy radiated into the basin as Rossby waves in the north. It should also be noted that the westward-propagating waves do not travel west of about 72°E which could be due to the presence of the Maldives island chain which lies off the southwest coast of India near this longitude and are oriented in the north-south direction.

[39] The strength and generation of equatorially trapped Kelvin waves are known to be influenced by zonal wind stress along the surface of the equatorial Ocean. It is also known that the MJO is strongly correlated with zonal wind in this region [*Madden and Julian*, 1972]. Many equatorial events evident in Figure 9 occur at times that correspond with large MJO events. Generally the best correspondence between MJO and sea level events occurs during late Boreal spring and summer (approximately from May to August). One particularly notable example of this is the summer of 1997. The westward-propagating waves along 5.5°N may be a combination of remote and local forcing. Figure 9 shows that they are often partly based on signals originating in the equatorial region and so are partially forced remotely by wind generated waves in the equatorial Indian Ocean. Note that the westward-propagating waves exhibit characteristics such as multiple wave speeds and amplification or decay along their paths that cannot be attributed solely to such remote forcing. Additional analysis (not shown) indicates that these waves are not strongly associated with zonal wind or wind stress curl along 5.5°N (as would be expected if they are locally forced Rossby waves). Clearly, a more detailed modeling study of this region is required in order to determine the dominant waveforms along with their forcing and decay.

6. Concluding Remarks

[40] The Madden-Julian Oscillation is the dominant mode of intraseasonal variability in the tropical atmosphere and we have shown, using satellite-based measurements of sea level, that it can have a significant effect on sea surface height. Using traditional statistics we have developed a simple scalar metric that allows us to measure the strength of the connection between the MJO and sea level variability in a given frequency band and at a fixed location. This metric has allowed us to map, for the first time, the connection between sea level and the MJO on a global scale. To help identify the physical processes, regional analyses have been performed using a frequency-dependent EOF analysis in order to identify the dominant modes of sea level variability in the MJO band.

[41] We used the global maps to identify regions which have a strong connection between sea level and the MJO by considering both statistical significance (the magnitude of the coherence) and practical significance (the magnitude of the predicted sea level response). The most significant regions include the equatorial Pacific Ocean and the west coast of the Americas (combined into one region), the shallow seas off the north coast of Australia (including the Gulf of Carpentaria and the Arafura and Timor Seas), and the northeastern Indian Ocean. These regions were examined individually in order to determine the dominant physical processes relevant for variability on MJO time scales.

[42] The equatorial Pacific and coastal Americas act as a continuous waveguide linking both equatorially and coastally trapped waves. Signals are forced by zonal surface winds in the western Pacific and then propagate east along the equator as Kelvin waves. Once they strike the American coast they they excite coastally trapped waves which then propagate poleward and are detected as far as 37°N and 33°S. The sea level variability north of Australia consists of a standing wave in the Gulf of Carpentaria and nearby shallow seas. Further investigation shows that most of the variability is due to sea level setup driven by local onshore winds associated with the MJO. Finally, the northeastern Indian Ocean exhibits a complex variety of different behaviors. We speculate that equatorially trapped Kelvin waves, generated by surface wind forcing (as in the equatorial Pacific), excite signals along the coasts of Sumatra that propagate poleward as coastal trapped waves and into the basin as Rossby waves that travel westward along 5.5°N.

[43] The present study relies on a combination of statistical analysis and simple physical interpretations (e.g., sea level setup due to wind based on linear theory as well as considerations of local and remote forcing). There are, however, some important questions to be answered. Does the wind-driven sea level setup in the Gulf of Carpentaria act as a generator of Rossby waves in the adjacent deep ocean as suggested by the small amplitude waves observed of the west coast of Australia? Is the fact that westward Rossby waves in the northeastern Indian Ocean are predominantly radiated along 5.5°N related to bathymetry or coastal geography? In order to answer such questions, and confirm the physical explanations given earlier, a more complex modeling study is required that includes realistic bathymetry, forcing and stratification. It would be useful to attempt to reproduce maps of $\bar{\kappa}$ using a global model. Higher-resolution regional models could be used to answer some of the questions given above and explore the physical processes in more detail. Future work will involve pursuing such a modeling study for both the Gulf of Carpentaria and the northeastern Indian Ocean regions.

[44] A deeper understanding of the dynamics could potentially lead to useful forecasting systems for coastal communities. For example, the detection of sea level anomalies in the western equatorial Pacific associated with an MJO event could act as a signal to forecasters of the

possibility of predictable coastal anomalies at a later date in the Americas. Furthermore, the passage of coastally trapped waves can lead to anomalies in ocean currents as well as temperature and salinity due to upwelling and downwelling.

[45] This study discusses the relationship between the Madden-Julian Oscillation and sea level variability in the global ocean. Sea level can be forced by the atmosphere but has little effect back on the atmosphere. If we wish to understand the relevance of two-way atmosphere-ocean interactions on the dynamics of the MJO the most logical oceanic property to examine is sea surface temperature [*Kessler et al.*, 1995; *Batstone et al.*, 2005; *Pohl and Matthews*, 2007]. In fact, results from a preliminary study of surface temperature indicate that there are regions of the extratropical ocean with significant connections to the MJO. These connections will be explored in more detail in a subsequent study.

Appendix A: Calculating $\bar{\kappa}$ and Measuring Statistical Significance

[46] The calculation of coherence outlined in section 3.1 was modified by adding a small constant to the power spectra of the MJO indices (effectively the same as adding a small amount of white noise to the original time series). In this way, the MJO power spectra are now nonzero at high frequencies and this reduces spurious large coherencies at high frequencies. This also allows us integrate over all frequencies rather than arbitrarily choosing a band of "MJO frequencies". In practice, this small constant offset is between one and five percent of the maximum in the power spectra of the MJO index.

[47] To assess the statistical significance of a particular value of $\bar{\kappa}^2$ we used a Monte Carlo technique under the assumption of no relationship between the variable of interest and the MJO. We generate clone time series of the MJO with the same mean, variance and spectral density but randomized phases (by manipulating and inverting its Fourier transform). Using a large number of cloned MJO time series a sample distribution for $\bar{\kappa}^2$ can be generated under the assumption of no relationship between the ocean variable and the MJO. The value of $\bar{\kappa}$ for which 95% of the distribution falls below is taken as the 5% significance level and denoted by $\bar{\kappa}_{5\%}$.

[48] **Acknowledgments.** E.C.J.O. would like to acknowledge the assistance provided by the following colleagues at Dalhousie University and the Bedford Institute of Oceanography (Xu Zhang, Youyu Lu, Simon Higginson, and Clark Richards). E.C.J.O. and K.R.T. further acknowledge the Global Ocean-Atmosphere Prediction and Predictability (GOAPP) research network and the Canadian Foundation for Climate and Atmospheric Sciences (CFCAS). K.R.T. also acknowledges financial support from the Discovery Grant program of the National Sciences and Engineering Research Council (NSERC) of Canada.

References

Batstone, C., A. Matthews, and D. Stevens (2005), Coupled ocean-atmosphere interactions between the Madden-Julian Oscillation and synoptic-scale variability over the warm pool, *J. Clim.*, *18*(12), 2004–2020.

Bond, N., and G. Vecchi (2003), The influence of the Madden-Julian Oscillation on precipitation in Oregon and Washington, *Weather Forecasting*, *18*(4), 600–613.

Brillinger, D. (2001), *Time Series: Data Analysis and Theory*, Soc. for Ind. Math., Philadelphia, Pa.

Brink, K. (1982), A comparison of long coastal trapped wave theory with observations off Peru, *J. Phys. Oceanogr.*, *12*(8), 897–913.

Cane, M., and E. Sarachik (1981), The response of a linear baroclinic equatorial ocean to periodic forcing, *J. Mar. Res.*, *39*, 651–693.

Cassou, C. (2008), Intraseasonal interaction between the Madden-Julian Oscillation and the North Atlantic Oscillation, *Nature*, *455*(7212), 523–527.

Cazenave, A., A. Lombard, and W. Llovel (2008), Present-day sea level rise: A synthesis, *C. R. Geosci.*, *340*(11), 761–770.

Chelton, D., R. de Szoeke, M. Schlax, K. El Naggar, and N. Siwertz (1998), Geographical variability of the first baroclinic Rossby radius of deformation, *J. Phys. Oceanogr.*, *28*(3), 433–460.

Chelton, D., M. Schlax, J. Lyman, and G. Johnson (2003), Equatorially trapped Rossby waves in the presence of meridionally sheared baroclinic flow in the Pacific Ocean, *Prog. Oceanogr.*, *56*(2), 323–380.

Clarke, A. (1977), Wind-forced linear and nonlinear Kelvin waves along an irregular coastline, *J. Fluid Mech.*, *83*(2), 337–348.

Clarke, A. (1992), Low-frequency reflection from a nonmeridional eastern ocean boundary and the use of coastal sea level to monitor eastern Pacific equatorial Kelvin waves, *J. Phys. Oceanogr.*, *22*(2), 163–183.

Clarke, A., and R. Ahmed (1999), Dynamics of remotely forced intraseasonal oscillations off the western coast of South America, *J. Phys. Oceanogr.*, *29*(2), 240–258.

Clarke, A., and X. Liu (1993), Observations and dynamics of semiannual and annual sea levels near the eastern equatorial Indian Ocean boundary, *J. Phys. Oceanogr.*, *23*(2), 386–399.

Clarke, A., and C. Shi (1991), Critical frequencies at ocean boundaries, *J. Geophys. Res.*, *96*(C6), 10,731–10,738.

Enfield, D. (1987), The intraseasonal oscillation in eastern Pacific Sea levels: How is it forced?, *J. Phys. Oceanogr.*, *17*(11), 1860–1876.

Fu, L. (2003), Wind-forced intraseasonal sea level variability of the extratropical oceans, *J. Phys. Oceanogr.*, *33*(2), 436–449.

Fu, L., E. Christensen, C. Yamarone Jr., M. Lefebvre, Y. Ménard, M. Dorrer, and P. Escudier (1994), TOPEX/POSEIDON mission overview, *J. Geophys. Res.*, *99*(C12), 24,369–24,382.

Gill, A. (1982), *Atmosphere-Ocean Dynamics*, Academic, San Diego, Calif.

Grimshaw, R., and J. Allen (1988), Low-frequency baroclinic waves off coastal boundaries, *J. Phys. Oceanogr.*, *18*(8), 1124–1143.

Hall, J., A. Matthews, and D. Karoly (2001), The modulation of tropical cyclone activity in the Australian region by the Madden-Julian Oscillation, *Mon. Weather Rev.*, *129*(12), 2970–2982.

Han, W., D. Lawrence, and P. Webster (2001), Dynamical response of equatorial Indian Ocean to intraseasonal winds: Zonal flow, *Geophys. Res. Lett.*, *28*(22), 4215–4218.

Hendon, H., B. Liebmann, and J. Glick (1998), Oceanic Kelvin Waves and the Madden-Julian Oscillation, *J. Atmos. Sci.*, *55*(1), 88–101.

Iskandar, I., W. Mardiansyah, Y. Masumoto, and T. Yamagata (2005), Intraseasonal Kelvin waves along the southern coast of Sumatra and Java, *J. Geophys. Res.*, *110*, C04013, doi:10.1029/2004JC002508.

Kessler, W., M. McPhaden, and K. Weickmann (1995), Forcing of intraseasonal Kelvin waves in the equatorial Pacific, *J. Geophys. Res.*, *100*(C6), 10,613–10,631.

Lin, H., G. Brunet, and J. Derome (2009), An observed connection between the North Atlantic Oscillation and the Madden-Julian Oscillation, *J. Clim.*, *22*, 364–380.

Madden, R., and P. Julian (1972), Description of global-scale circulation cells in the tropics with a 40–50 day period, *J. Atmos. Sci.*, *29*(6), 1109–1123.

Maloney, E., and D. Hartmann (2000a), Modulation of eastern North Pacific hurricanes by the Madden-Julian Oscillation, *J. Clim.*, *13*(9), 1451–1460.

Maloney, E., and D. Hartmann (2000b), Modulation of hurricane activity in the Gulf of Mexico by the Madden-Julian Oscillation, *Science*, *287*(5460), 2002–2004.

Meehl, G., G. Kiladis, K. Weickmann, M. Wheeler, D. Gutzler, and G. Compo (1996), Modulation of equatorial subseasonal convective episodes by tropical-extratropical interaction in the Indian and Pacific Ocean regions, *J. Geophys. Res.*, *101*, 15,033–15,050.

Moore, D., and J. McCreary (1990), Excitation of intermediate-frequency equatorial waves at a western ocean boundary: With application to observations from the Indian Ocean, *J. Geophys. Res.*, *95*, 5219–5231.

Pohl, B., and A. Matthews (2007), Observed changes in the lifetime and amplitude of the Madden-Julian Oscillation associated with interannual ENSO sea surface temperature anomalies, *J. Clim.*, *20*(11), 2659–2674.

Sengupta, D., R. Senan, and B. Goswami (2001), Origin of intraseasonal variability of circulation in the tropical central Indian Ocean, *Geophys. Res. Lett*, *28*(7), 1267–1270.

Shinoda, T., H. Hendon, and J. Glick (1998), Intraseasonal variability of surface fluxes and sea surface temperature in the tropical western Pacific and Indian oceans, *J. Clim.*, *11*(7), 1685–1702.

Spillane, M., D. Enfield, and J. Allen (1987), Intraseasonal oscillations in sea level along the west coast of the Americas, *J. Phys. Oceanogr.*, *17*(3), 313–325.

Thompson, K., R. Marsden, and D. Wright (1983), Estimation of low-frequency wind stress fluctuations over the open ocean, *J. Phys. Oceanogr.*, *13*(6), 1003–1011.

Vecchi, G., and N. Bond (2004), The Madden-Julian Oscillation (MJO) and northern high latitude wintertime surface air temperatures, *Geophys. Res. Lett.*, *31*, L04104, doi:10.1029/2003GL018645.

Waliser, D. (2005), Predictability and forecasting, in *Intraseasonal Variability in the Atmosphere-Ocean Climate System*, edited by W. K. M. Lau and D. E. Waliser, pp. 389–423, Springer, Berlin.

Wallace, J., and R. Dickinson (1972), Empirical orthogonal representation of time series in the frequency domain. Part I: Theoretical considerations, *J. Appl. Meteorol.*, *11*(6), 887–892.

Wheeler, M. C., and H. H. Hendon (2004), An all-season real-time multivariate MJO index: Development of an index for monitoring and prediction, *Mon. Weather Rev.*, *132*(8), 1917–1932.

Wheeler, M., and G. Kiladis (1999), Convectively coupled equatorial waves: Analysis of clouds and temperature in the wavenumber–Frequency domain, *J. Atmos. Sci.*, *56*(3), 374–399.

Woolnough, S., J. Slingo, and B. Hoskins (2000), The relationship between convection and sea surface temperature on intraseasonal timescales, *J. Clim.*, *13*(12), 2086–2104.

Zhang, C. (2005), Madden-Julian Oscillation, *Rev. Geophys*, *43*, 1–36.

Zhang, X., Y. Lu, and K. Thompson (2009), Sea level variations in the tropical Pacific Ocean and the Madden-Julian Oscillation, *J. Phys. Ocean.*, *39*, 1984–1992.

E. C. J. Oliver and K. R. Thompson, Department of Oceanography, Dalhousie University, 1355 Oxford St., Halifax, NS B3H 4JI, Canada. (eric.oliver@phys.ocean.dal.ca; keith.thompson@dal.ca)